

Article

# Detection of Residual “Hot Spots” in RFI-Filtered SMAP Data

Yan Soldo <sup>1,2,\*</sup>, David Le Vine <sup>1</sup>  and Paolo de Matthaeis <sup>1,2</sup>

<sup>1</sup> NASA Goddard Space Flight Center, 8800 Greenbelt Road, Greenbelt, MD 20770, USA; david.m.levine@nasa.gov (D.L.V.); paolo.dematthaeis@nasa.gov (P.d.M.)

<sup>2</sup> Universities Space Research Association, 7178 Columbia Gateway drive, Columbia, MD 21046, USA

\* Correspondence: yan.soldo@nasa.gov

Received: 8 November 2019; Accepted: 4 December 2019; Published: 7 December 2019



**Abstract:** Radio frequency interference (RFI) is a well-documented problem for passive remote sensing of the Earth at L-band even though the measurements are made in the protected band at 1.413 GHz. Consequently, filtering for RFI is an important early step in the processing of measurements made by the SMAP (Soil Moisture Active/Passive) radiometer. However, the filtered data still include regions with suspiciously high antenna temperatures. One possible cause of these “hot spots” is interference not fully detected during RFI filtering. This paper presents evidence supporting this hypothesis and describes an algorithm to identify these “hot spots” so that they can be removed from the measurements. The impact of removing these “hot spots” is generally small, but evidence is presented that the brightness temperature and soil moisture improve when the hot spots are removed.

**Keywords:** SMAP; interference; RFI detection

## 1. Introduction

### 1.1. SMAP

SMAP (Soil Moisture Active/Passive) is a satellite mission to provide global maps of soil moisture and the freeze/thaw state of the surface by measuring radiation from the Earth’s surface at L-band. The instrument consists of a conically scanning radiometer operating in the 1400–1427 MHz band reserved for passive use only [1,2]. A unique feature of SMAP is the fully polarimetric measurements and digital receiver backend that permits advanced processing of data [3,4].

Although SMAP operates in a band where no transmission is allowed [5], the measurements are affected by radio-frequency interference (RFI) [6–8]. For the purpose of RFI detection, SMAP data are divided into two data streams [3]. One is called “full-band”, and in this stream, the data have an integration time of about 0.3 ms over the full instrument bandwidth of 24 MHz. In the other data stream, called “sub-band”, the 24 MHz bandwidth is divided into 16 sub-bands of 1.5 MHz with an integration time of 1.2 ms in each band. The data are collected into “footprints”. In time-frequency space, a footprint is 9.6 ms long (i.e.,  $8 \times 1.2$  s) and 24 MHz wide ( $16 \times 1.5$  MHz). Footprints are reported every 16.8 ms (which also includes the time for internal calibration).

This is outlined in Section 1.2 below.

### 1.2. RFI Detection Criteria Used in SMAP

The full-band and sub-band data streams are processed for RFI independently with different criteria in each stream. Signals meeting any of the criteria are identified as RFI and are removed from the subsequent processing. When full-band samples (0.3 ms long) are identified as affected by RFI, the entire 1.2 ms samples containing them are removed [9]. The criteria applied to each of the data

streams to identify signals corrupted by RFI are described in [3]. Briefly, the following are used in the full-band data stream

- Time-domain outlier detection;
- High absolute values of the third and fourth Stokes parameters;
- Kurtosis values different from 3.

In the sub-band data stream, the individual sub-bands are also compared in the frequency domain and outliers are removed.

Figure 1 shows a footprint in time-frequency before and after RFI detection. In the left panel, high antenna temperature associated with RFI is visible in channel 7–9. In the right panel, the flagged samples have been blanked (removed) and appear in dark blue. The SMAP data processor uses these two spectrograms to compute two values that are then included in the L1B data: “Ta”, which corresponds to the antenna temperature before RFI mitigation and is the average of all samples within the spectrogram (i.e., left panel), and “Ta\_filtered”, which is the average of the all the non-flagged samples in the spectrogram (i.e., right panel) [9]. A metric for RFI contamination for each footprint, called “RFI percentage”, is defined as the percentage of samples that were flagged as RFI.

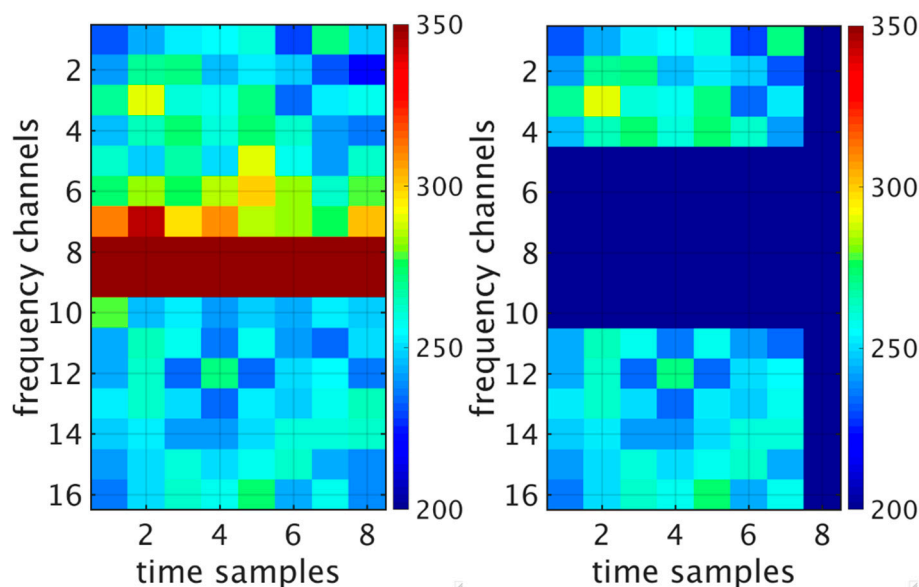


**Figure 1.** Spectrogram showing Ta (antenna temperature) of an SMAP footprint. The footprint consists of radiometer measurements, each 1.2 s long (horizontal axis) and each consisting of 16 sub-bands (vertical axis) that are 1.5 MHz wide. Hence, each square is 1.5 MHz  $\times$  1.2 s in time-frequency space. The figure on the left is before RFI mitigation (detection and removal), and after mitigation is shown on the right. The samples identified as RFI have been blanked and appear in dark blue on the right.

### 1.3. “Hot Spots” in the Filtered Antenna Temperature

Even after the RFI detection process is implemented by SMAP, the Ta\_filtered data still show some small regions where the temperature is suspiciously higher than the surrounding areas. One possible cause for these “hot spots” is that RFI was not entirely detected by the SMAP algorithm. This happens because each criterion involves thresholds which are chosen as a compromise between maximizing detection and minimizing false alarms; however, other explanations are possible. For example, urban areas in the field of view could raise the brightness temperature of the scene. This was considered as a potential cause for the “hot spots”, but no significant correlation has been found. To the authors’ knowledge, no naturally occurring phenomenon (e.g., craters of active volcanoes) can explain the significant number of the “hot spots” being observed. RFI appears to be the most likely cause. Some evidence is available to support this hypothesis. For example, some of the “hot spots” vary rapidly in

time (they appear and disappear in a matter of days), and the “hot spots” that are more stable in time correspond to locations where SMOS (Soil Moisture Ocean Salinity, another spaceborne instrument operating in the same frequency band) detected high levels of RFI contamination. A more detailed discussion about the evidence that supports this hypothesis is included in Section 4.

An example of a hot spot is presented in Figure 2. Figure 2 reports  $T_a$ \_filtered in the vicinity of Turkey for an orbit on 7 July 2017, with a “hot spot” near Ankara, Turkey (left panel). The panels on the right show the spectrograms for 14 footprints in the location of the “hot spot”. The spectrograms correspond to a portion of the scan during which the radiometer boresight crossed the location of the “hot spot”. The top right panel shows  $T_a$  (i.e., before RFI mitigation), and the bottom is  $T_a$ \_filtered. The “hot spot” is clearly visible between samples 40–80. As can be seen in the bottom right panel, several samples (dark blue) have been flagged as RFI. Although the detection algorithm has some false alarms, the number of flagged samples is higher near the “hot spot” than elsewhere, suggesting that at least part of the “hot spot” was identified as containing RFI by the detection algorithm. The vertical lines indicated RFI was detected by the full-band processor. After RFI detection (bottom panel), a signal significantly higher than the surrounding regions persists.

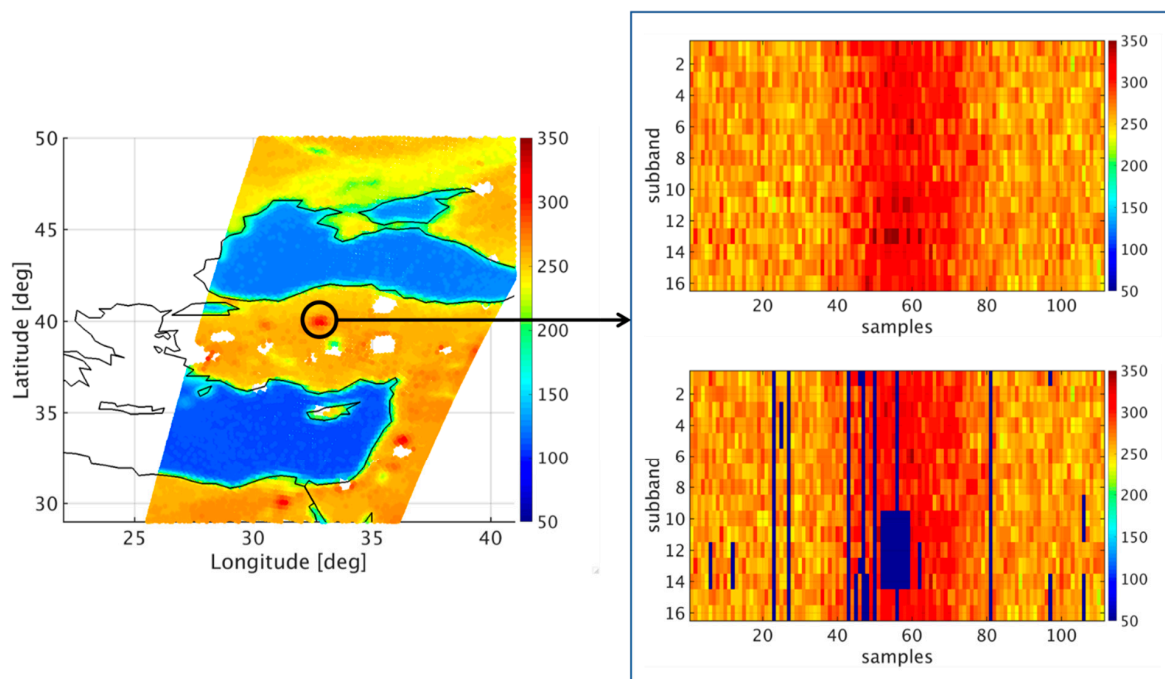


**Figure 2.** Example of RFI source in Turkey that was not entirely detected. The spectrograms represent the time series of the sub-band data stream as the radiometer moves toward the RFI location and then away from it. The dark blue region on the right indicates the portion of the spectrogram that was identified as RFI.

## 2. Materials and Methods

An algorithm is proposed here to identify outliers such as those shown in Figure 2. The algorithm is applied to SMAP antenna temperature after correction for RFI,  $T_a$ \_filtered, as reported in the L1B data files. The algorithm is applied to each individual half orbit independently as described in the following paragraphs as well as in the flow chart in Figure 3. The steps outlined in this section may be applied multiple times to the same half orbit until no more “hot spots” are identified.

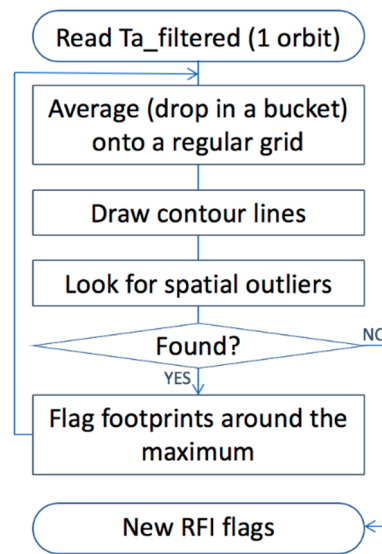


Figure 3. Flow chart of the proposed algorithm.

### 2.1. Binning

The latitude and longitude given in the L1B files are the intersection point of the boresight ray and the Earth's surface. The first step of this algorithm consists of binning the L1B data (which are in the native format associated with the conical scan) into a fixed  $0.25 \times 0.25$  degree rectangular grid. The value assigned to each grid cell is the average of the  $T_{a\_filtered}$  of each footprint whose boresight is within that grid cell.

### 2.2. Definition of Iso-Lines at Fixed Temperatures

The second step consists of defining contour lines corresponding to fixed values of antenna temperatures,  $T_{A,k} = 200 + 5k$ , where  $k = \{0, 1, 2, \dots\}$ . That is,  $T_{A,k}$  is increased in steps of 5 K starting at 200 K and ending at  $T_{A,k} \leq \max(T_{A,grid})$ , where  $T_{A,grid}$  represents the gridded values of  $T_{a\_filtered}$ . Values of  $T_{A,k}$  below 200 K correspond to footprints with a substantial water fraction; these regions were not processed to reduce the computation time.

The algorithm used to draw the iso-lines (the *contour* Matlab built-in function) considers the binned values of  $T_{a\_filtered}$  as the vertices of a series of squares. Given a specific value of antenna temperature ( $T_1$ ) for which a contour line is desired, the *contour* function searches each edge of each square to see if  $T_1$  is between the values at the vertices associated with that edge. When that is the case, the contour line will cross that edge. The exact point of the crossing is computed with a linear interpolation between the value  $T_1$  and the binned values of  $T_{a\_filtered}$  associated with that edge. Doing so for all the edges in the grid yields a series of points (between vertices). The contour line (or iso-line) is the line passing through all those points [10].

At the end of this step, the algorithm has defined a series of contour lines corresponding to the values of  $T_k$ . Figure 4 shows the map of the original  $T_{a\_filtered}$  (left) and the corresponding contour lines of the gridded product (right) for orbit 12,981.

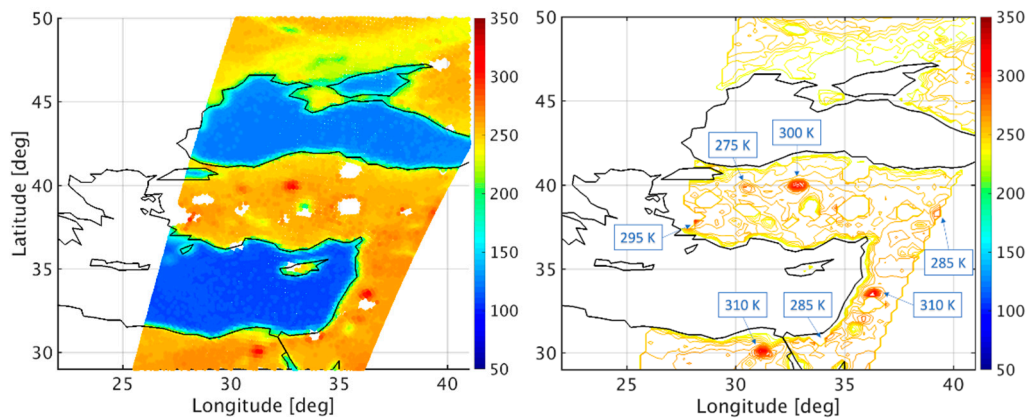


**Figure 4.** Map of the  $T_a$ \_filtered (vertical polarization) for SMAP orbit 12981 with several “hot spots”. The left panel shows all the maps of the original individual footprints, while the right panel shows the iso-line contours for the corresponding gridded data.

### 2.3. Identification of Local Maxima

The next step is designed to identify the specific contour line corresponding to a “hot spot”. The selection is done using three criteria:

- The contour line has to correspond to a local maximum;
- The ratio between the area enclosed by the adjacent contour line and the area enclosed by the contour line under consideration has to be less than 1.5;
- The average of the RFI percentage reported by the SMAP algorithm and obtained from all the footprints associated with the area inside the contour line has to be greater than 10%.

The value “1.5” for the second criterion was selected by trial-and-error by applying this algorithm to several orbits. Values too low for this parameter lead to no “hot spot” being detected, and values too high lead to local maxima with low gradients of temperature possibly being selected as potential “hot spots”. In the third criterion, “10%” was chosen considering that the RFI detection false alarm rate is approximately 6.3% and that the standard deviation of the RFI percentage in a region expected to be RFI-free is approximately 0.5% (i.e., 10% is larger than the false alarm but small enough that RFI could have been missed).

### 2.4. Flagging

Once the contour lines corresponding to “hot spots” are identified, the algorithm flags the footprint corresponding to the location of the local maximum temperature as well as all footprints that are within 20 km of the local maximum (the SMAP 3 dB resolution is about 40 km [11]; hence, half a resolution cell).

The outputs of this algorithm are two flags (one for each polarization), which are applied to the footprints. These flags are applied to  $T_a$ \_filtered. Figure 5 shows a map of  $T_a$ \_filtered for the same half-orbit as in Figure 4 after removal of the footprints that were flagged by the algorithm.

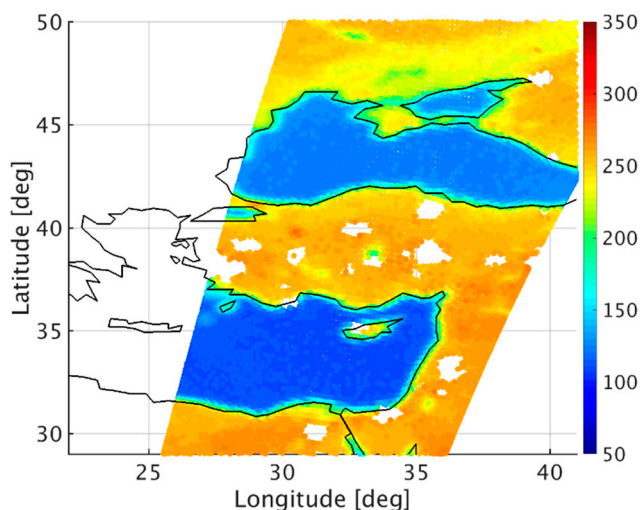


**Figure 5.** Map of the  $Ta_{\text{filtered}}$  (vertical polarization) for the same SMAP orbit, where the footprints flagged by the proposed new flag have been discarded.

It is possible that the feature near  $40^{\circ}\text{N}$ ,  $30^{\circ}\text{E}$  is also a “hot spot”. However, that feature was associated with an RFI percentage lower than 10% and it was therefore not flagged by this algorithm.

### 3. Results

#### 3.1. Max-Hold Maps

One way of assessing the impact of this algorithm is to examine max-hold maps of  $Ta_{\text{filtered}}$  (i.e., maps where each  $0.25 \times 0.25$  degree cell is filled with the maximum  $Ta_{\text{filtered}}$  among the footprints whose center was within that cell). Figure 6 shows some examples of max-hold maps, computed using data from the period from 1 August 2018 to 31 August 2018 for parts of the world known to be associated with RFI (e.g., [7,12,13]). The left panels are computed without accounting for the new flag. The middle panels are computed discarding the footprints that were flagged by the new flag. The right panels show the difference, in Kelvin, between the left and the middle panels.

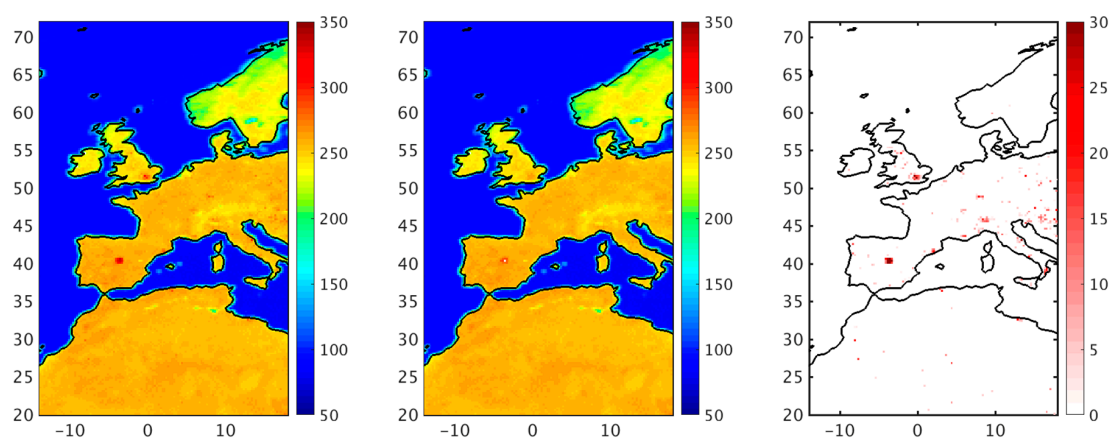


**Figure 6.** Cont.

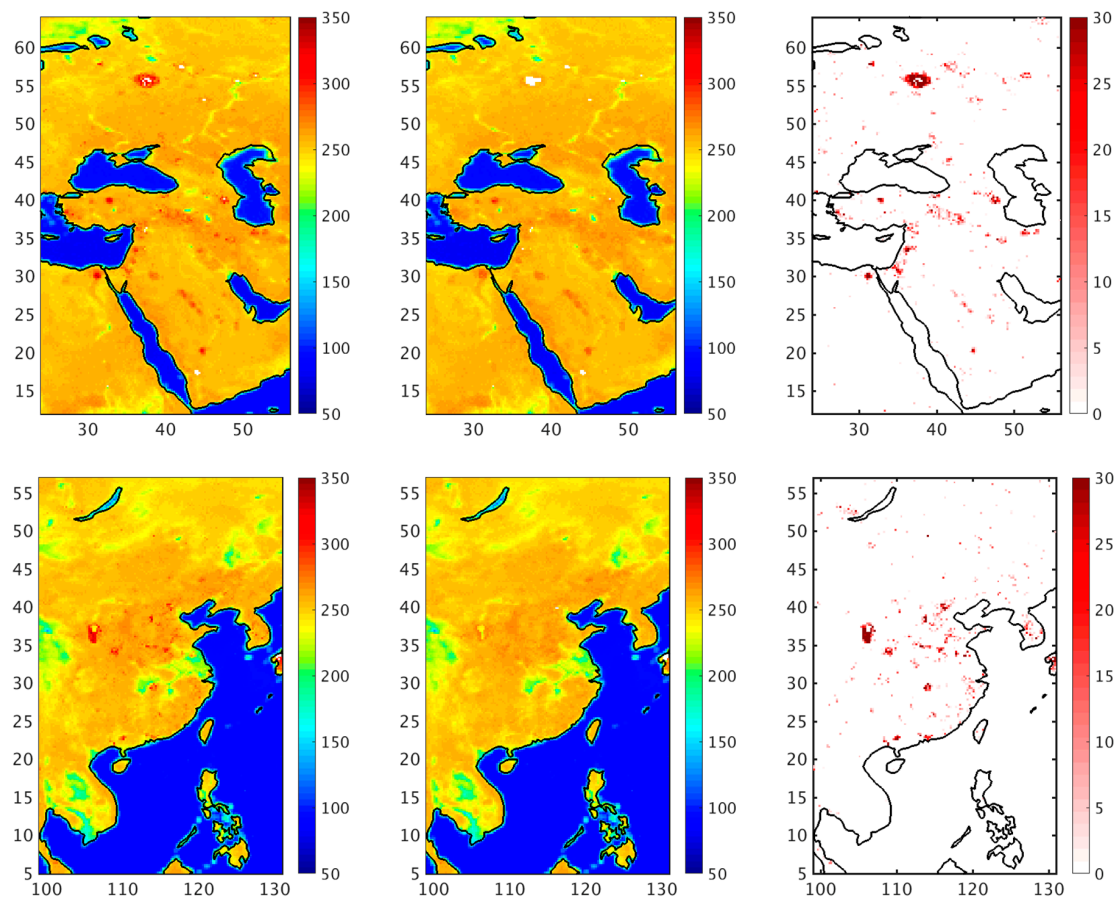


**Figure 6.** Max-hold map for the period 1–31 August 2018 using a  $0.25 \times 0.25$  degree grid. The maps on the left were obtained using the measured  $T_a$  after RFI filtering. The maps in the middle were obtained in the same way, but the footprints flagged by the proposed flag were discarded. On the right is the difference map between the left and the middle panels.

The effect of the new flag is visible in the difference maps (right panel). Figure 6 shows that the new flag provides some improvement to the max-hold maps. Hot spots appear very clearly on the left panels (e.g., in Turkey and in Spain) but they are fewer and with smaller amplitude in the middle panels. The proposed algorithm also seems to help flagging footprints near RFI sources that were already removed by the RFI detection (e.g., near Moscow). The map of Saudi Arabia (middle plot) still has features that resemble hot spots (near  $20^\circ\text{N}$ ,  $45^\circ\text{E}$ ); in this case, the temperatures are decreased by the new flag, but the area still appears slightly warmer than the surrounding area in the max-hold plot, which indicates that the proposed algorithm does not flag every region that appears suspicious to the human eye, and some missed detections are to be expected even after applying both this algorithm and the regular SMAP RFI detection algorithm.

### 3.2. Statistical Considerations for the TB Data

Another way of assessing the effect of this new flag is through statistical metrics on higher-level data products. In this section, we will focus on brightness temperature TB (and in Section 3.3 on soil moisture). The data used are the TB-reported L1C products.

In order to make this kind of assessment, the SMAP footprints are re-gridded into a regular grid (36 km EASE 2 grid), following the same procedure used to create the SMAP L1C files from L1B files [14]. This procedure consists of determining which footprints have centers within a particular grid cell and then assigning to the grid cell the weighted average of those footprints. The weights used in the average are the inverse squared distances (computed along great circles) between the footprint

center and the center of the grid cell. The average is then normalized using the sum of all the inverse squared distances.

The output of this procedure is two datasets of brightness temperature: one does not use the new proposed flag and it is very similar to the official L1C product released by the SMAP mission; the other reads the proposed new flag and discards all the footprints flagged by it. Discarding the flagged footprints can lead to two scenarios: if only some of the footprints within the cell are discarded, the cell has a value of TB that is different than that of the current L1C files; whereas if all the footprints within an EASE 2 grid are discarded, that grid cell remains empty (no TB is assigned to it and soil moisture retrieval in that grid is prevented).

In the SMAP processing, there are flags associated with the EASE2 grid cells that indicate conditions unfavorable to the retrieval of soil moisture. These flags, called “surface flags” in the SMAP L2 products, are raised, for example, if the fraction of urban area is high or if the grid cell is near a coast line, or in the case of frozen ground, dense vegetation or mountainous terrain. More information on these flags can be found in [15]. Depending on these flags, the soil moisture retrieval is attempted or not, and the retrieved soil moisture is determined to be of “recommended quality” or of “uncertain quality”. In this section, we will only consider grid cells where all “surface flags” are set to 0, which indicates good quality.

The data used for the following analysis correspond to the first 8 days of August 2018. In this period, accounting for the proposed flags modified the TB of 1497 grid cells (4147, if the existence of surface flags had not already ruled these cells out) and removed the TB from 101 grid cells (1062, without accounting for the surface flags).

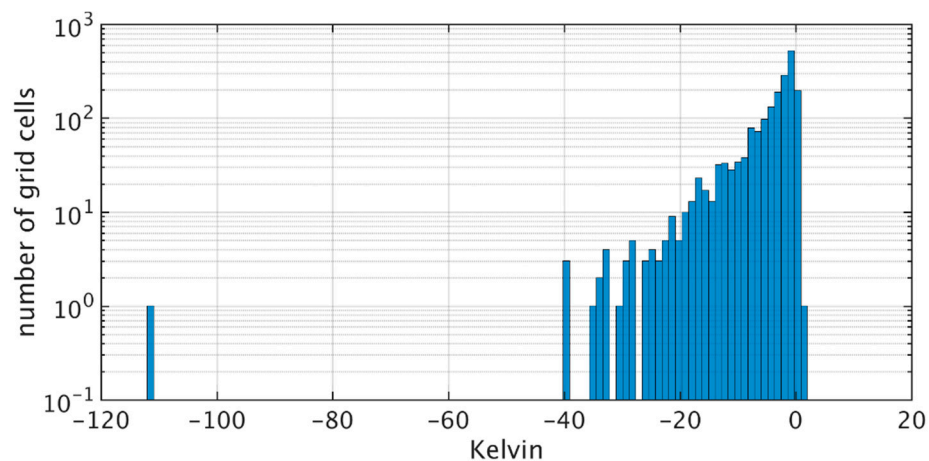
### 3.2.1. Cases in Which the Brightness Temperature in the Grid Cell Was Modified but Not Removed.

As a first assessment, we consider the cases in which the gridded TB has been modified but not removed. In particular, we consider two aspects: how the TB in the EASE 2 grid cells changes because of the proposed flag and how the standard deviation in the affected area changes with and without the flag.

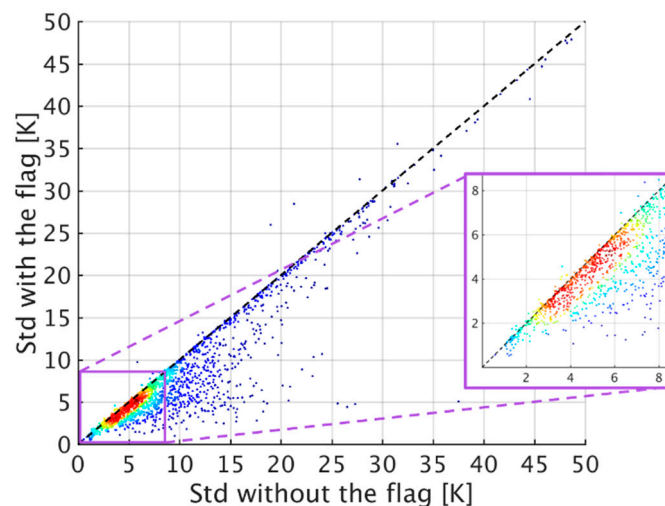
Figure 7 is a histogram of the difference between the datasets with and without the new flag. Negative values on the  $x$ -axis indicate that the TB in the grid cell decreases when accounting for the proposed flag. The bar near  $-110$  K (extreme left on the histogram) corresponds to a region of India with low natural brightness temperatures (around 230 K) where RFI was detected and removed by the SMAP algorithm although one pixel with anomalously large temperature remained. Many of the larger negative values in Figure 7 correspond to Japan, where RFI was attributed to a problem with TV broadcast receivers covering very large areas and appears, in some respect, similar to thermal noise [16]. The two cases with positive values occurred when the flagged footprints did not correspond to the maxima within those cells. This can occur because when a footprint is flagged; all the footprints within a 20 km radius are also flagged. Figure 7 shows that the predominant effect of the proposed flag is to remove large values and thus to decrease the average brightness temperatures associated with EASE 2 grid cells.

Figure 8 shows how the standard deviation is affected by the proposed flag. The standard deviation is computed using the grid cell whose TB was modified by the proposed flag and the 8 neighboring grid cells.

In Figure 8, the  $x$ -axis is the original standard deviation, and on the  $y$ -axis is the standard deviation after discarding the flagged footprint. The color indicates the density of data points. In the vast majority of the cases, the standard deviation decreases when applying the proposed flag. This indicates that the high values removed from the grid cells tend to be outliers. The data points with very high standard deviations tended to be near coastlines.



**Figure 7.** Histogram of the change in the L1C TBs with and without the new flag. Negative values indicate that using the new flag decreases the TB in the L1C files.

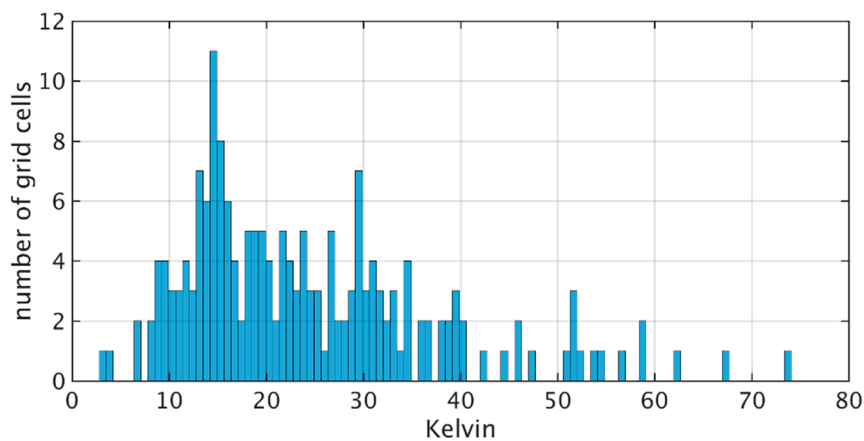


**Figure 8.** Density plot of the standard deviations computed in the areas around the grid cells with the modified TBs. The standard deviation on the  $x$ -axis is before applying the new flag, whereas the standard deviation on the  $y$ -axis is computed after applying it.

### 3.2.2. Comparison between the Removed TB and the Other TBs in Its Vicinity

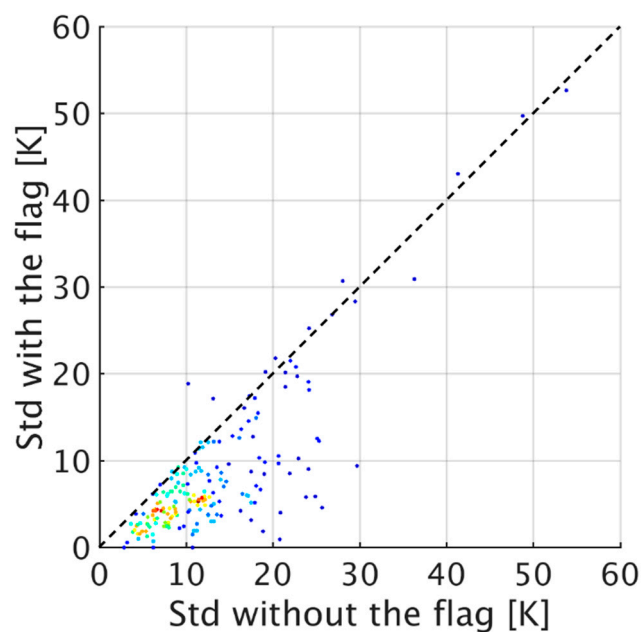
In this paragraph, we focus on the instances in which applying the proposed flag creates grid cells with no valid footprints inside them and therefore do not have an associated TB. In this case, we compare the “removed TB” (i.e., the TB that the grid cells have without the new flag) and the average TB obtained from the 8 grid cells surrounding the now empty cell.

Figure 9 is a histogram of the difference between the original TB and the average TB of the 8 neighboring cells. As in Figure 7, the histogram shows that the TB of the footprints removed was higher than the average of the nearby footprints. The large differences do not necessarily indicate large TB. For example, the largest differences correspond to pixels near coast lines, where the average of the neighboring TB is low. This figure also shows that the “removed TBs” were always above the local average.



**Figure 9.** Histogram of the difference between the original TB that was removed and the average TB in the neighboring cells. A positive difference means that the original TB is larger than the average of the surrounding pixels.

Figure 10 compares the standard deviation of the TBs in the affected region (8 grid cells surrounding the grid cell with flagged footprints) with and without the proposed flag and is similar to the data shown in Figure 8 for the case when some footprints remain. Again, it shows that applying the new flag decreases the standard deviation in the majority of cases.



**Figure 10.** Density plot of the standard deviations computed in the areas around the grid cells of the “removed TBs”. The standard deviation of the  $x$ -axis does not account for the new flag, whereas the standard deviation on the  $y$ -axis accounts for it.

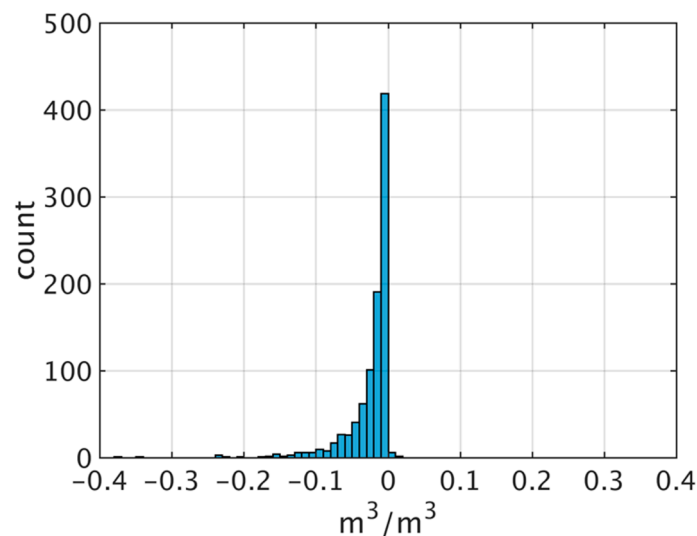
### 3.3. Statistical Considerations of the Effect of the New Flag on the Retrieved Soil Moisture

Data flagged with this algorithm were also used to produce an 8-day soil moisture dataset using the operational SMAP processing algorithm. This soil moisture is identical to the regular SMAP products except for the locations where the new flag was raised. The effect of the new flag can be either to modify the retrieved soil moisture (SM) or to removed it entirely (if all the underlying footprints were flagged).

### 3.3.1. Cases in Which the Soil Moisture Was Modified but Not Removed

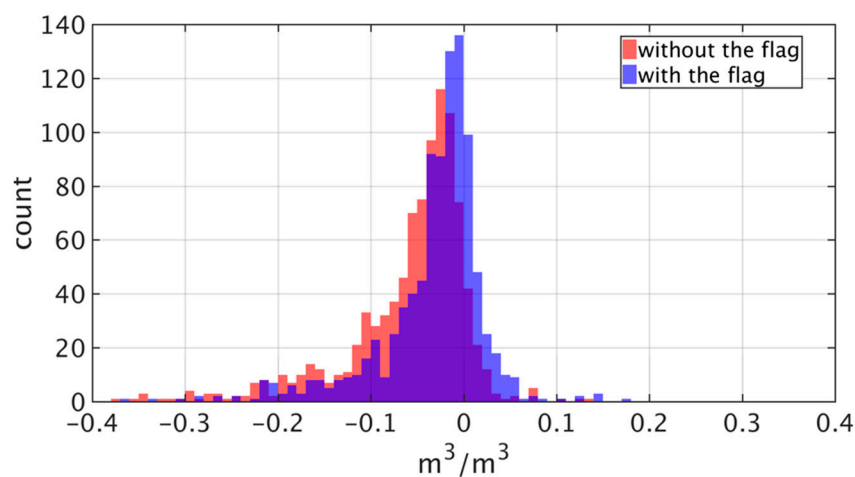
Over the 8 days, 1110 values of soil moisture were modified but not removed. For context, there were approximately  $8 \cdot 10^5$  valid soil moisture values in the same dataset. Of these 1110 values, 126 were listed as “unsuccessful retrievals” in the original retrieval (i.e., without the new flag), and this number was reduced to 64 with the new flag.

Figure 11 shows how much the SM values changed when applying the flag. The 5th, 50th, and 95th percentiles of this distribution are  $-0.090$ ,  $-0.012$ , and  $-0.002 \text{ m}^3/\text{m}^3$ , respectively. In other words, the change in soil moisture is small, and the new soil moisture values are slightly wetter (which corresponds to a lower TB).



**Figure 11.** Histogram of the difference between the SM with and without the new flag. Negative values indicate that using the new flag increases the soil moisture (lowers TB).

Also, we compared the soil moisture values against the average soil moisture in their vicinity. The red histogram in Figure 12 shows the difference between the original SM values and the average SM in their vicinity. The blue histogram is the same quantity but with the modified SM instead of the original SM. It appears that without the new flag, the SM values were slightly drier than the surrounding SM. With the new flag, the histogram is more centered at zero, suggesting that the SM is more similar to the neighboring values.



**Figure 12.** Histogram of the difference between the SM in the cells affected by the new flag and the average SM in their surrounding areas. Negative values indicate that SM is drier than its surroundings.

Using the new flag also reduces the standard deviation of SM in the affected areas. This is shown in Figure 13, which compares the standard deviation (Std) of the affected cell and the eight surrounding neighbors before modification (without the flag) and after modification (with the flag). In the vast majority of cases, the Std is reduced, again confirming that the flag identifies outliers.

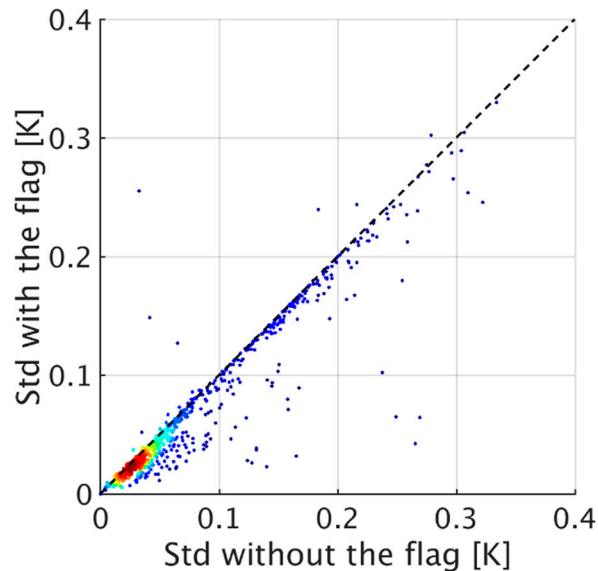


**Figure 13.** Density plot of the standard deviation computed in the areas around the cells with modified SM.

### 3.3.2. Cases in Which the Soil Moisture Values Were Removed

In the 8-day period, 533 values of SM were removed because of the new flag. Of these, 367 were already marked as “unsuccessful retrievals” in the standard product. For the remaining 166, we compared the removed values with the average SM in their vicinity. This is reported in Figure 14, which is a histogram of the difference between the removed SM and the average of the eight neighboring cells. Except in a few cases, the removed SMs were drier than the surrounding values of SM, and for those that were wetter, the difference was very small ( $0.05 \text{ m}^3/\text{m}^3$ ). On the other hand, the SM of the drier cells removed was as high as  $0.7 \text{ m}^3/\text{m}^3$ .

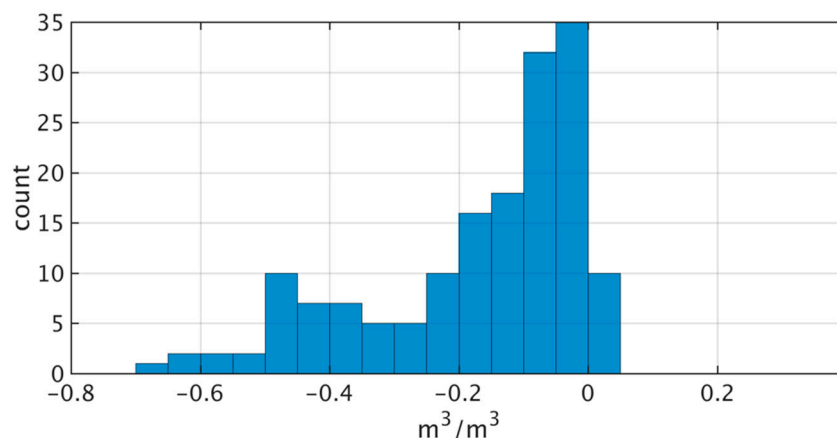


**Figure 14.** Histogram of the difference between the removed SM and the average SM in their neighboring cells.

The standard deviation of SM in the 8 neighboring grid cells was reduced after the new flag was applied. This is reported in Figure 15, which shows a scatter plot comparing the standard deviations

computed using the 8 cells surrounding the grid cell of the “removed TBs” including the removed cell (without flag) and omitting the removed cell (with flag). The standard deviation of the x-axis was computed before applying the flag, and the y-axis is the Std after removing the affected cell.

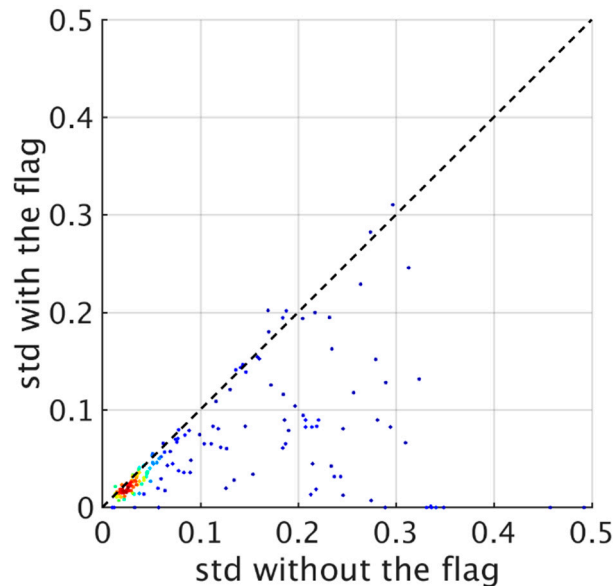


**Figure 15.** Density plot of the standard deviation computed in the areas around the grid cells where the SM was removed by the new flag.

#### 4. Discussion

The question remains as to the cause of these hot spots. One source of warmer than expected brightness temperature is the presence of urban development (i.e., man-made structures). However, we compared the location of the hot spots with a map of urban development (from the GRUMP dataset, available at <https://sedac.ciesin.columbia.edu/data/set/grump-v1-urban-extents>) and found no significant correlation. Another hypothesis is that they are the result of RFI missed by the SMAP algorithm. The same hypothesis was reported in [17]. There is some evidence to support this hypothesis. The presence of RFI above the level of the false alarm was one of the criterion associated with identifying the hot spots, so we know that RFI is present at some level (e.g., Figure 2). Some additional evidence is presented below.

##### 4.1. Comparison with RFI Detected from SMOS

One indication that RFI may have been missed is that other satellites (SMOS in this case) have detected RFI at these locations using algorithms different from those employed by SMAP. For example, Figure 16 shows maps of the RFI percentage from SMOS (left panel) and from SMAP (right panel) for the first 8 days of July 2017. For SMOS, the RFI percentage is computed on the 1.2 s measurements corresponding to each discrete global grid point (the grid used in SMOS Level 1C and Level 2 products) [18]. The map on the right for SMAP was obtained by regridding the footprints to a fixed  $0.25 \times 0.25$  degree grid and assigning to each grid cell the average RFI percentage of the footprints within that cell. The location indicated by the black circle indicates the hot spot shown in Figure 2. The RFI percentage in that location is approximately 80% for SMOS and 30% for SMAP. The RFI detection algorithm used by SMOS is quite different from the one used by SMAP, and in principle, the SMAP detector is more advanced. However, the SMOS algorithm employs criteria which might, in this case, have detected RFI missed by SMAP. The criteria that SMOS uses are tests for (1) the stability of the first Stokes parameter as a function of incidence angles; (2) the difference between the measured brightness temperatures and expected brightness temperatures; and (3) the presence of outliers in the angular signature of brightness temperatures [18,19].

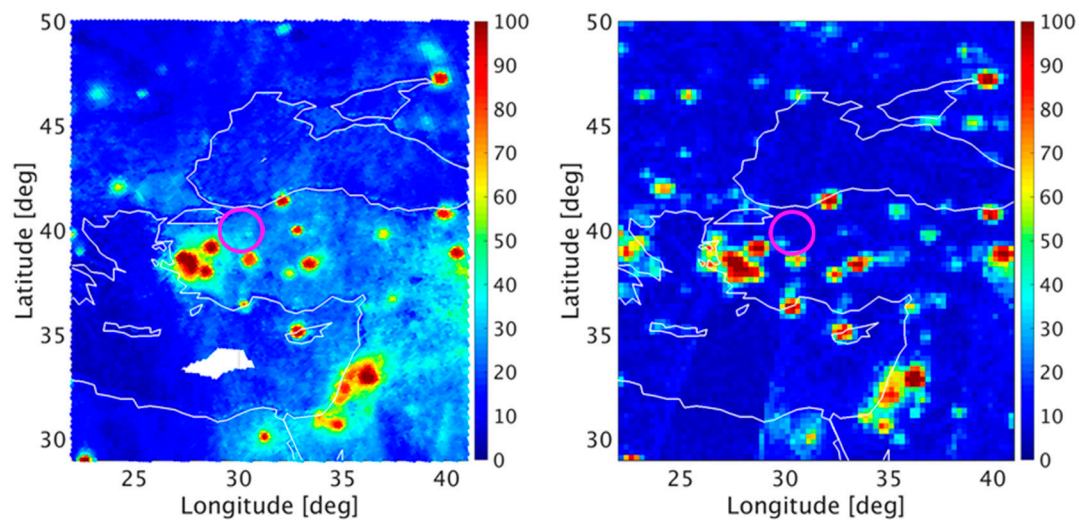


**Figure 16.** Maps of RFI percentage from SMOS (left) and from SMAP (right) over the same period. The location of the RFI in Figure 2 is highlighted here by a purple circle. That location corresponds to an approximate RFI percentage of 80% in SMOS and about 30% in SMAP.

#### 4.2. Natural Variability of $T_a$ Over Land

Another indication that the “hot spots” might be caused by RFI is the steep variation of  $T_a$  in their vicinity.

One way to quantify the variation of  $T_a$  is to compute its gradient in space as the ratio of the difference in  $T_a$  between two points to the distance between them. Computing the gradient of  $T_a$  for an 8-day period (1–8 July 2017) and keeping only the footprints over land (fraction of water in the field of view 1%) and those not affected by RFI (RFI percent equal to or less than the false alarm rate) yields the statistical distribution in Figure 17 for “natural” surfaces. The standard deviations for V- and H-pol are 0.057 and 0.069 K/km, respectively. On the other hand, the maximum gradients near the “hot spot” in Ankara for the orbit on 6 August 2018 are approximately ten times larger: 0.604 (V-pol) and 0.622 (H-pol) K/km. These much larger values at the hot spot suggest that natural variability of  $T_a$  is not likely to be the cause of this “hot spot”.

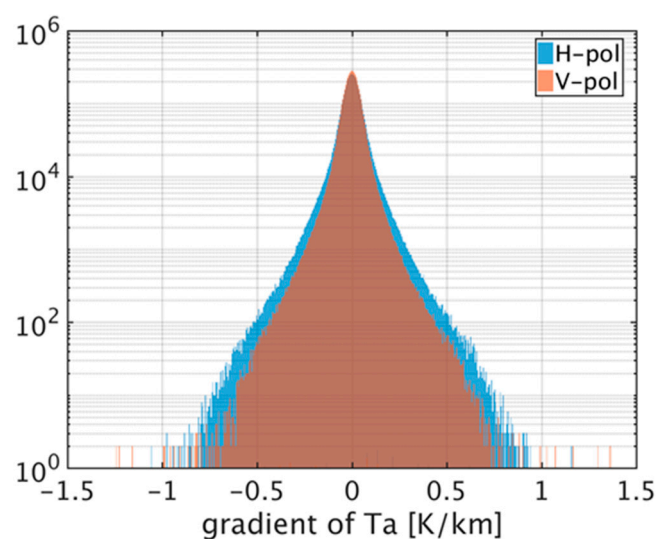


**Figure 17.** Statistical distribution of the gradient of  $T_a$  (in V- and H-pol) for the RFI-free footprints over land and for the period 1–8 July 2017.

### 4.3. Variations in Time

The “hot spots” are also not necessarily stable in time. Figure 18 shows max-hold maps with and without accounting for the new flag, as well as the difference between the two, for different 3-day periods between 18 August 2018 and 30 August 2018. A 3-day period corresponds to the shortest time for which there are no gaps in the maps. Clearly, different “hot spots” appear in some time frames but not in others. This is consistent with RFI emissions not being entirely detected (RFI is known to be not necessarily stable in time), and it also indicates that “hot spots” are most likely not due to certain surface characteristics such as the fraction of urban surfaces that do not vary significantly at this time scale.

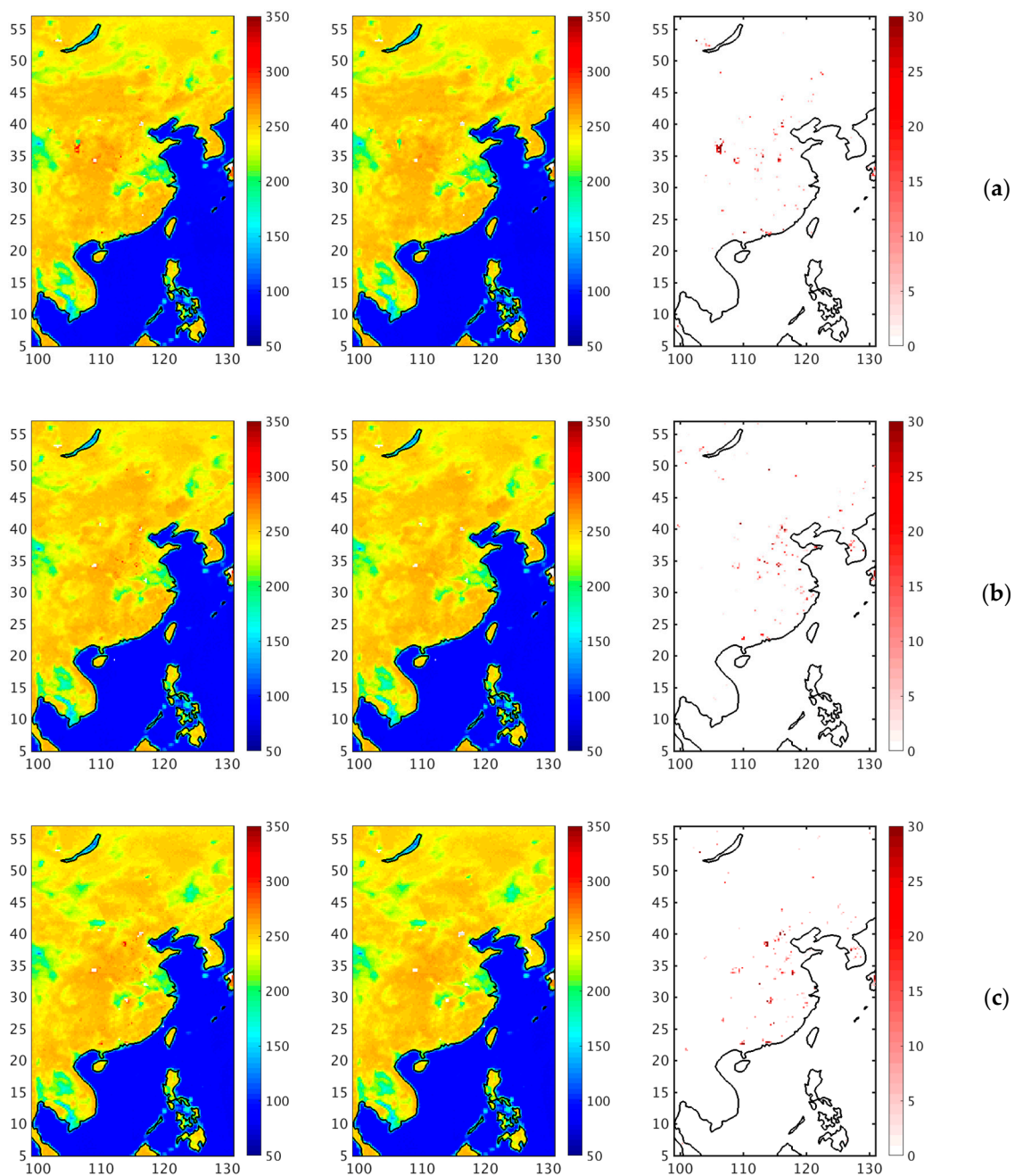
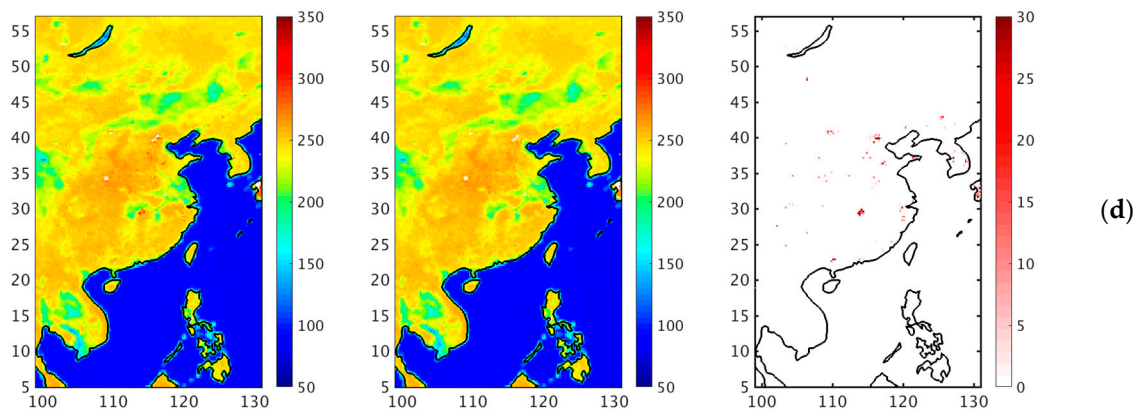


Figure 18. Cont.



**Figure 18.** Variations of the “hot spots” in time. Similar to Figure 5, in the left column are the max-hold maps using the  $T_a$  after RFI filtering; in the middle column are the max-hold maps after removing the footprints flagged by the new algorithm; and in the right column are the difference maps. Different rows correspond to different time frames: (a) 18–21 August 2018; (b) 22–24 August; (c) 25–27 August; (d) 28–30 August.

#### 4.4. Missed RFI Detections in Aquarius

A similar issue of missed RFI detection was also addressed by the Aquarius mission: among the RFI-filtered antenna temperatures in the Aquarius products, some had unusually high values and corresponded to locations of RFI detected by the SMOS mission, which suggested residual RFI contamination [16]. To address this, the Aquarius team included in their processing an additional RFI flag that was computed from the comparison between the RFI-filtered antenna temperature and a simplified land emissivity model. The land emissivity model provides an estimate of the highest antenna temperature that can be expected from the natural scene at the incidence angles of the Aquarius beams and for H- and V-pol. The new flag was raised whenever the RFI-filtered antenna temperatures were higher than the values from the emissivity model. After implementing this new flag, the maps of RFI detection by Aquarius and SMOS over Japan became more consistent [16], thus supporting the hypothesis that there was in fact residual RFI contamination.

Although Aquarius used a less sophisticated RFI detection strategy (a time-domain outlier detection algorithm [20]), the fact that residual RFI contamination was present in Aquarius is further indication of the difficulty in detecting certain kinds of RFI sources that appear similar to the thermal noise emitted by natural sources.

## 5. Conclusions

The RFI detection strategy currently implemented by SMAP is state-of-the-art for L-band radiometry. The advanced technology (fully polarimetric receiver and digital processing) allows SMAP to employ multiple algorithms in time and frequency space simultaneously. However, regions of anomalously high brightness temperature are present. An algorithm was presented here to identify these hot spots and to remove them prior to processing the data to retrieve soil moisture. The algorithm is applied separately for vertical and horizontal polarization and results in a flag identifying potentially corrupt footprints.

An assessment of the effect of these new flags showed that using them to remove footprints removes outliers in max-hold maps of  $T_{a\_filtered}$  (a common indicator of RFI [21]) and improves the comparison of TB in the affected cells with the TB in the neighboring cells. The new flags were also evaluated by comparing the SM in the current SMAP products with an 8-day ad-hoc dataset of SM obtained by applying the SMAP operational processing to the flagged data. From this comparison it was shown that using the new flags would modify or remove very few SM values, but that the SM values that were modified by the new flag yielded a greater number of successful SM retrievals.

The effect was to lower the standard deviation of SM in the areas affected by the new flags and to yield new SM values that have a smaller dry-bias compared to the SM in neighboring cells.

While the cause of the hot spots is not known, a reasonable hypothesis is that they are caused by RFI not detected by the SMAP algorithm. Evidence to support this hypothesis was presented in Section 3. While the cause of the “hot spots” is important to drive future improvements of the detection technology, it is not really relevant to the retrieval of soil moisture. This new flag decreases failed retrievals and improves the consistency of the retrieval. We hope research will continue on the reason for the hotspots, but in the meantime, we believe that implementing the proposed algorithm to flag and remove footprints before producing scientific products (soil moisture) will improve the quality of the data distributed by the SMAP mission.

**Author Contributions:** Y.S. and D.L.V. carried out the investigation. Y.S. prepared the original draft. All authors reviewed and edited the text.

**Funding:** This research was funded by the National Aeronautics and Space Administration (NASA) through the GESTAR Cooperative Agreement No. NNG11HP16A with Universities Space Research Association (USRA). The article processing charges were waived by the publisher.

**Conflicts of Interest:** The authors declare no conflict of interest.

## References

- Entekhabi, D.; Njoku, E.G.; O'Neill, P.E.; Kellogg, K.H.; Crow, W.T.; Edelstein, W.N.; Entin, J.K.; Goodman, S.D.; Jackson, T.J.; Johnson, J.; et al. The soil moisture active passive (SMAP) mission. *Proc. IEEE* **2010**, *98*, 704–716. [[CrossRef](#)]
- Entekhabi, D.; Yueh, S.; O'Neill, P.E.; Kellogg, K.H.; Allen, A.; Bindlish, R.; Brown, M.; Chan, S.; Colliander, A.; Crow, W.T.; et al. *SMAP Handbook-soil Moisture Active Passive: Mapping Soil Moisture and Freeze/Thaw From Space*; JPL Publication: Pasadena, CA, USA, 2014.
- Piepmeyer, J.R.; Johnson, J.T.; Mohammed, P.N.; Bradley, D.; Ruf, C.; Aksoy, M.; Garcia, R.; Hudson, D.; Miles, L.; Wong, M. Radio-frequency interference mitigation for the soil moisture active passive microwave radiometer. *IEEE Trans. Geosci. Remote Sens.* **2014**, *52*, 761–775. [[CrossRef](#)]
- Misra, S.; Johnson, J.; Aksoy, M.; Peng, J.; Bradley, D.; O'Dwyer, I.; Padmanabhan, S.; Dawson, D.; Chazanoff, S.; Latham, B.; et al. SMAP RFI mitigation algorithm performance characterization using airborne high-rate direct-sampled SMAPVEX 2012 data. In Proceedings of the IEEE International Geoscience and Remote Sensing Symposium-IGARSS, Melbourne, Australia, 21–26 July 2013; pp. 41–44.
- International Telecommunication Union. *Radio Regulations*; International Telecommunication Union: Geneva, Switzerland, 2016; pp. 101–102.
- Piepmeyer, J.R.; Focardi, P.; Horgan, K.A.; Knuble, J.; Ehsan, N.; Lucey, J.; Brambora, C.; Brown, P.R.; Hoffman, P.J.; French, R.T.; et al. SMAP L-band microwave radiometer: Instrument design and first year on orbit. *IEEE Trans. Geosci. Remote Sens.* **2017**, *55*, 1954–1966. [[CrossRef](#)]
- Soldo, Y.; Le Vine, D.M.; Bringer, A.; de Mattheais, P.; Oliva, R.; Johnson, J.T.; Piepmeyer, J.R. Location of Radio-Frequency Interference Sources Using the SMAP L-Band Radiometer. *IEEE Trans. Geosci. Remote Sens.* **2018**, *56*, 6854–6866. [[CrossRef](#)]
- Soldo, Y.; Le Vine, D.M.; Bringer, A.; Mohammed-Tano, P.M.; de Mattheais, P.; Piepmeyer, J.R.; Johnson, J.T. Recent Advances in SMAP RFI Processing. In Proceedings of the Geoscience and Remote Sensing Symposium (IGARSS), 2018 IEEE International, Valencia, Spain, 22–27 July 2018; pp. 123–124.
- Piepmeyer, J.; Mohammed, P.; De Amici, G.; Kim, E.; Peng, J.; Ruf, C. *Algorithm Theor. Basis Doc., SMAP L1B Radiom. Bright. Temp. Data Product.: L1B\_TB (Rev. B)*; NASA Goddard Space Flight Center: Greenbelt, MD, USA, 2016; pp. 16–23.
- Matlab®-Graphics-R2012a. *Mathworks*, 2012; 5.73–5.76.
- Font, J.; Ballabrera-Poy, J.; Camps, A.; Corbella, I.; Duffo, N.; Duran, I.; Emelianov, M.; Enrique, L.; Fernández, P.; Gabarró, C.; et al. A new space technology for ocean observation: the SMOS mission. *Sci. Mar.* **2012**, *76*, 249–259.

12. Le Vine, D.M.; Lagerloef, G.S.E.; Ruf, C.; Wentz, F.; Yueh, S.; Piepmeier, J.; Lindstrom, E.; Dinnat, E. Aquarius: The instrument and initial results. In Proceedings of the 2012 IEEE 12th Specialist Meeting on Microwave Radiometry and Remote Sensing of the Environment (MicroRad), Frascati, Italy, 5–9 March 2012.
13. Kristensen, S.S.; Balling, J.; Skou, N.; Søbjerg, S.S. RFI in SMOS data detected by polarimetry. In Proceedings of the IEEE International Geoscience and Remote Sensing Symposium, Munich, Germany, 22–27 July 2012; pp. 3320–3323.
14. Chan, S.; Njoku, E.; Colliander, A. *Algorithm Theoretical Basis Document, Level 1C Radiometer Data Product (Rev. A)*; Jet Propulsion Laboratory: Pasadena, CA, USA, 2014; pp. 12–17.
15. O'Neill, P.; Binlish, R.; Chan, S.; Njoku, E.; Jackson, T. *Algorithm Theoretical Basis Document, Level 2 3 Soil Moisture (Passive) Data Product (Rev. D)*; Jet Propulsion Laboratory: Pasadena, CA, USA, 2018.
16. Soldo, Y.; de Mattheais, P.; Le Vine, D.M. L-band RFI in Japan. In *Radio Frequency Interference (RFI)*; IEEE: Piscataway, NJ, USA, 2016; pp. 111–114.
17. Bringer, A.; Johnson, J.T.; Mohammed, P.N.; Piepmeier, J.R. Performance of SMAP radiometer RFI detection algorithms and analysis of residual RFI sources. In Proceedings of the IEEE International Geoscience and Remote Sensing Symposium (IGARSS), Fort Worth, TX, USA, 23–28 July 2017; pp. 1243–1246.
18. Soldo, Y.; Le Vine, D.M.; de Mattheais, P.; Richaume, P. L-band RFI detected by SMOS and Aquarius. *IEEE Trans. Geosci. Remote Sens.* **2017**, *55*, 4220–4235. [[CrossRef](#)]
19. *SMOS Project: SMOS Level 2 Processor Soil Moisture Algorithm Theoretical Basis Document*; ARGANS/ACRI: Plymouth, UK, 2011; Revision 5, Sections 3, Issue 3.
20. Le Vine, D.M.; de Mattheais, P.; Ruf, C.S.; Chen, D.D. Aquarius RFI detection and mitigation algorithm: Assessment and examples. *IEEE Trans. Geosci. Remote Sens.* **2013**, *52*, 4574–4584. [[CrossRef](#)]
21. Aksoy, M.; Johnson, J.T. A study of SMOS RFI over North America. *IEEE Geosci. Remote. Sens. Lett.* **2012**, *10*, 515–519. [[CrossRef](#)]



© 2019 by the authors. Licensee MDPI, Basel, Switzerland. This article is an open access article distributed under the terms and conditions of the Creative Commons Attribution (CC BY) license (<http://creativecommons.org/licenses/by/4.0/>).